

Journal of Materials Chemistry A

Ultra-stable and poison tolerance oxygen evolution activity enabled by surface In2O3-x(OH)y of Co3In2S2 large single-crystal

Journal:	Journal of Materials Chemistry A
Manuscript ID	TA-ART-07-2024-004608.R1
Article Type:	Paper
Date Submitted by the Author:	13-Sep-2024
Complete List of Authors:	Sheelam, Anjaiah; Washington State University, Chemistry; University of Illinois at Urbana-Champaign, Materials Science and Engineering Whitten, Ariel; Washington State University Moore, Carrington; Washington State University Engelhard, Mark; Pacific Northwest National laboratory, Environmental Molecular Sciences Laboratory McEwen, Jean-Sabin; Washington State University, Chemical Engineering and Bioengineering Bell, Jeffrey; Washington State University, Chemistry

SCHOLARONE™ Manuscripts

ARTICLE

Ultra-stable and poison tolerance oxygen evolution activity enabled by surface In₂O_{3-x}(OH)_y of Co₃In₂S₂ large single-crystal

Received 00th January 20xx, Accepted 00th January 20xx

DOI: 10.1039/x0xx00000x

Anjaiah Sheelam,^a Ariel Whitten,^{b, =} Carrington Gates Moore,^{b, =} Mark Engelhard,^c Jean-Sabin McEwen,^{a,b,d,e,f} and Jeffrey G. Bell^{a,b} *

Water is an earth-abundant source for clean hydrogen production via electrochemical water electrolysis (WE). However, the surface poisoning that occurs in aqueous electrolytes drastically deactivates the electrocatalytic performance of electrodes. Here, we report an electrochemically formed $In_2O_{3-x}(OH)_y$ on the surface of a large (1–1.5 mm long, 0.5–0.6 mm wide and 0.3–0.5 mm thick) single-crystal of Weyl semimetal $Co_3In_2S_2$ ($Co_3In_2S_2/In_2O_{3-x}(OH)_y$) as an ultra-stable and poison tolerance electrode for the oxygen evolution reaction (OER) in 1 M KOH, addressing a bottleneck in WE. The OER activity of powder form of $Co_3In_2S_2$ is limited by its aerophilic nature. Remarkably, the single-crystal electrodes maintained their high activity for a continuous operational period of 5 h in 1 M KOH electrolyte with/without 10 mM of strong surface-poisoning ligands i.e., potassium cyanide, bipyridine, and ethylenediaminetetraacetate disodium salt. The electrodes exhibited stable OER activity for 1000 h at 100 mA cm⁻² (1.73 V vs. RHE). The temperature-dependent OER polarization curves (10–70 °C) unambiguously revealed surface poisoning through the suppression of precatalytic Co-redox peaks on the bipyridine poisoned electrode and lead to the stabilization of surface Co-sites. The X-ray photoelectron spectroscopy analyses of pristine, poisoned and post-electrocatalytic single-crystal $Co_3In_2S_2$ electrodes revealed the existence of $In_2O_{3-x}(OH)_y$ surface phase, which could be the potential heterostructure for the origin of ultra-stable and poison tolerance OER activity.

1. Introduction

The oxygen evolution reaction (OER; $40 H^- \rightarrow 0_2 + 2 H_2 O + 4 e^-$, $E^\circ = 1.229 \, \text{V}$ vs. reversible hydrogen electrode, RHE) is the anodic half-reaction in water electrolysers, and is identified as the efficiency bottleneck in producing clean and sustainable fuel *i.e.*, hydrogen, at the cathode. At present, Ir and Ru-based materials stand as the most efficient OER electrocatalysts. Nevertheless, their extensive adoption in grid-scale energy conversion devices faces significant constraints not only due to their high cost and scarcity but also their weak tolerance (<1 h) to surface-poisoning/corrosive ligands and instability at high anodic potentials (> 1 V vs. RHE). Thus far, cost and energy-intensiveness have been partially addressed through the advancement of efficient electrocatalysts based on earth-

abundant metals, such as transition-metal (oxy)hydroxides,5,6 sulfides 7-9 and heterostructures of phosphides/sulfides 10, 11. Industrial level water electrolysis (WE) performance (240 h at 300 mA cm⁻², 80 °C) was achieved by rare-earth modified NiS₂ electrocatalyst. 12 The rare-earth modification enhanced the OH coverage by improving the active site density. Transition-metals are relatively reactive, both in terms of chemical and electrochemical due to the strong degree of adsorption of various chemical species and multiple oxidation states, respectively. Normally, electrocatalysts fail to function if the electrolytes contain surface poisoning matter such as potassium cyanide (KCN)¹³ potassium thiocyanide (KSCN),^{14, 15} corrosive seawater (CIO⁻ is a corrosive by-product in chloride oxidation reaction),3,4 and ethylenediaminetetraacetate disodium salts (EDTA)¹⁵. Consequently, ultra-high pure water-based electrolytes are required to retain the electrocatalytic performance of transition-metal-based electrocatalysts, which is the key constraint for the realization of inexpensive and sustainable WE. Therefore, finding ultra-stable and poison tolerant metal-based electrocatalysts is crucial to enable economical and industrial-scale water electrolysers and other environmentally friendly electrochemical devices such as fuel cells and metal-air batteries.

In general, surface poison problems have been circumvented by developing metal-free electrocatalysts, particularly N-doped carbon-based materials for the oxygen reduction reaction. $^{\rm 15-18}$ However, carbon-based electrocatalysts exhibit repulsive interaction with $\rm H_2O$ and $\rm OH^-$ species, and

^a Department of Chemistry, Washington State University, Pullman, Washington 99164, United States.

b. The Gene and Linda Voiland School of Chemical Engineering and Bioengineering, Washington State University, Washington 99164, United States.

^c Environmental Molecular Sciences Laboratory, Pacific Northwest National Laboratory, Innovation Blvd, Richland-99354, Washington, United States.

d-Institute for Integrated Catalysis, Pacific Northwest National Laboratory,

Innovation Blvd, Richland-99354, Washington, United States.

e Department of Physics and Astronomy, Washington State University, Washington

^{99164,} United States.

f Department of Biological Systems Engineering, Washington State University,

Washington 99164, United States.
† Electronic Supplementary Information (ESI) available: [details of any supplementary information available should be included here]. See DOI: 10.1039/x0xx00000x

⁼ equal contributors: Ariel Whitten and Carrington Gates Moore

high-positive potentials trigger the carbon corrosion. ¹⁹ Consequently, metal-free alkaline OER catalysts are rarely found in the literature. ²⁰⁻²³ Identifying poison-tolerant metalbased OER electrocatalysts proves to be an additional challenge, with limited viable options.

Recently, a new class of materials, i.e., topological materials, have received intensive attention in electrocatalysis (e.g., OER,²⁴⁻²⁶ hydrogen evolution reaction,^{27, 28} oxygen reduction reaction,²⁹ and carbon dioxide reduction reaction³⁰) due to their extraordinary transport properties, high carrier density and topologically protected surface states (TSS). Large-size singlecrystals of the topological Weyl semimetal (TWS) Co₃Sn₂S₂ (4 mm long and 1.2 mm wide)²⁴ and the nodal line semimetal CoS₂ (2 mm long and 1.5 mm wide)²⁶ have been reported as promising catalysts for alkaline OER. At higher positive potentials (>1 V) the surface of transition metal-based catalysts tends to form (oxy)hydroxides and oxides in strong alkaline conditions. The compact interface Co_3O_4/CoS_2 formed on the bulk CoS₂ single-crystals is identified as the active structure in OER. Although the high electrical conductivity of topological materials appears to be a promising prerequisite for precatalysts, the well-known surface transformation (e.g., singlecrystal of Co₃Sn₂S₂) has not been documented so far. Initially, Co₃In₂S₂ was considered to be an uninteresting material due to the absence of a ferromagnetic order. Nevertheless, the electronic structure of Co₃In₂S₂ was found to host a pair of Weyl points around 0.5 eV below the Fermi level.31 Consequently, the high electronic conductivity of Co₃In₂S₂ appears to be a promising feature for boosting charge-transport property.

In this work, large-size single-crystals (1-1.5 mm long, 0.5-0.6 mm wide and 0.3-0.5 mm thick) of Co₃ln₂S₂ were prepared by the chemical vapor deposition method and employed as substrate-free electrodes for OER in 1 M KOH electrolyte at 22 ± 2 °C. The electrodes exhibited excellent durability over 1000 h at 100 mA cm⁻² without significant change in the overpotential. Remarkably, the OER activity endured 10 mM of strong surfacepoisoning ligands i.e., KCN, bipyridine (bpy), and EDTA contained in 1 M KOH. High-resolution X-ray photoelectron spectroscopy (XPS) data confirmed the surface poisoning of Co₃In₂S₂ single-crystal electrode. The coordination of bpy ligand to the Co-site blocked the surface oxidation of Co(OH)₂ to Cooxide/(oxy)hydroxide phase, but not the OER activity. The electrocatalytic performance, electrochemical impedance spectroscopy and X-ray photoelectron spectroscopy analyses of single-crystal Co₃In₂S₂ electrodes revealed the existence of In₂O_{3-x}(OH)_v surface phase, which could be the potential heterostructure for the origin of ultra-stable and poison tolerance OER activity. Furthermore, the facile adsorption energy of HOO intermediate on In2, In1, Co and Co-In1 calculated from density functional theory (DFT), rationalized the In2-site as the most facile site over Co- and/or In1-sites (the presence of two different In-sites is clarified in section '2.1 Crystal structure'), which might be the source for the electrochemical oxidation that led to the formation of $Co_3In_2S_2/In_2O_{3-x}(OH)_y$ heterostructure.

2. Results and discussion

2.1 Crystal structure. The temperature program outlined in Scheme S1 was implemented in the chemical vapor transport method to synthesize single-crystals of Co₃In₂S₂. Its crystal structure was confirmed using single-crystal X-ray diffraction (SC-XRD) analysis. It belongs to the Shandite family and crystallized in structure with $R\overline{3}m$ space group and rhombohedral crystal structure. Rietveld refinement was also carried out on the powder X-ray diffraction (XRD) pattern, to obtain crystal structure and lattice parameters (Fig. S1(a) and (b)). Thus, obtained lattice parameters are, a = b = 5.311 Å, c =13.650 Å and $\alpha = \beta = 90^{\circ}$ and $\gamma = 120^{\circ}$. The lattice parameters obtained from SC-XRD and Rietveld refinement were wellmatched with the reported lattice parameters (Table S1).31 Its crystal structure shows the corner (In1-site) shared Cooctahedra, S₂—Co—(In1)₂(In2)₂, connectivity along the z-axis. The In1-atoms (on the Kagome lattice) and In2-atoms (in between the Kagome lattice) reside in different chemical environments as shown in Fig. S1(c). The elemental composition of as-prepared single-crystal Co₃In₂S₂ was confirmed to be Co₃In_{2.05}S_{1.96} from the EDS analysis (Fig. S2). The ideal electronic configuration of the Shandite family is expected to be $(Co^{0})_{3}(In^{2+})_{2}(S^{2-})_{2}.^{32}$

2.2 Electrochemical performance. To the evaluate electrocatalytic alkaline OER of Co₃In₂S₂, cyclic voltammetry (CV) and electrochemical impedance spectroscopy (EIS) measurements were carried out on its single-crystal state and powder form. To attain the facile mass transport and removal of O₂-gas bubbles either the electrode (Powder/GC electrode set to 1000 rpm) or electrolyte (in the case of single-crystal electrode, the rotation rate of magnetic pellet set to 500 rpm) were subjected to forced convection. The OER current density of single-crystal Co₃In₂S₂ was normalized with its geometric area, 0.0053 cm², which was calculated from scanning electron microscopy (SEM) images (Fig. 1(a), details of the electrode fabrication process are provided in supporting information, Scheme S2). The single-crystal electrode exhibited 100 mA cm⁻² at an overpotential (η) of 500 mV, whereas IrO₂ and RuO₂ nanocatalysts have been reported to display only at η = 420 (10 mA cm⁻² at η = 285 mV)³³ and 361 mV (10 mA cm⁻² at η = 281 mV), 10 respectively. The ferromagnetic TWS Co₃Sn₂S₂ has been reported to exhibit a 390 mV overpotential at the same current density.²⁴ In an attempt to further decrease the overpotential by increasing the exposed surface area and number of active sites of Co₃In₂S₂, the single-crystal (1.3 mg) was ground to powder form and dispersed in 0.5 mL of isopropyl alcohol solvent. Various amounts of powder Co₃In₂S₂ were supported on a glassy carbon (Powder/GC) electrode to conduct the same analysis. The average size of Co₃In₂S₂ particles on GC is calculated to be 0.83 µm (Fig. 1(b)). The area occupied by $Co_3In_2S_2$ particles on the GC electrode (21 % = 0.015 cm², as observed using a SEM image) was considered the actual geometric area of Powder/GC (Fig. S3). The mass loading of powder Co₃In₂S₂ on GC was optimized to be 260 μg cm⁻² (Fig. S4). The OER polarization curves of single-crystal, Powder/GC

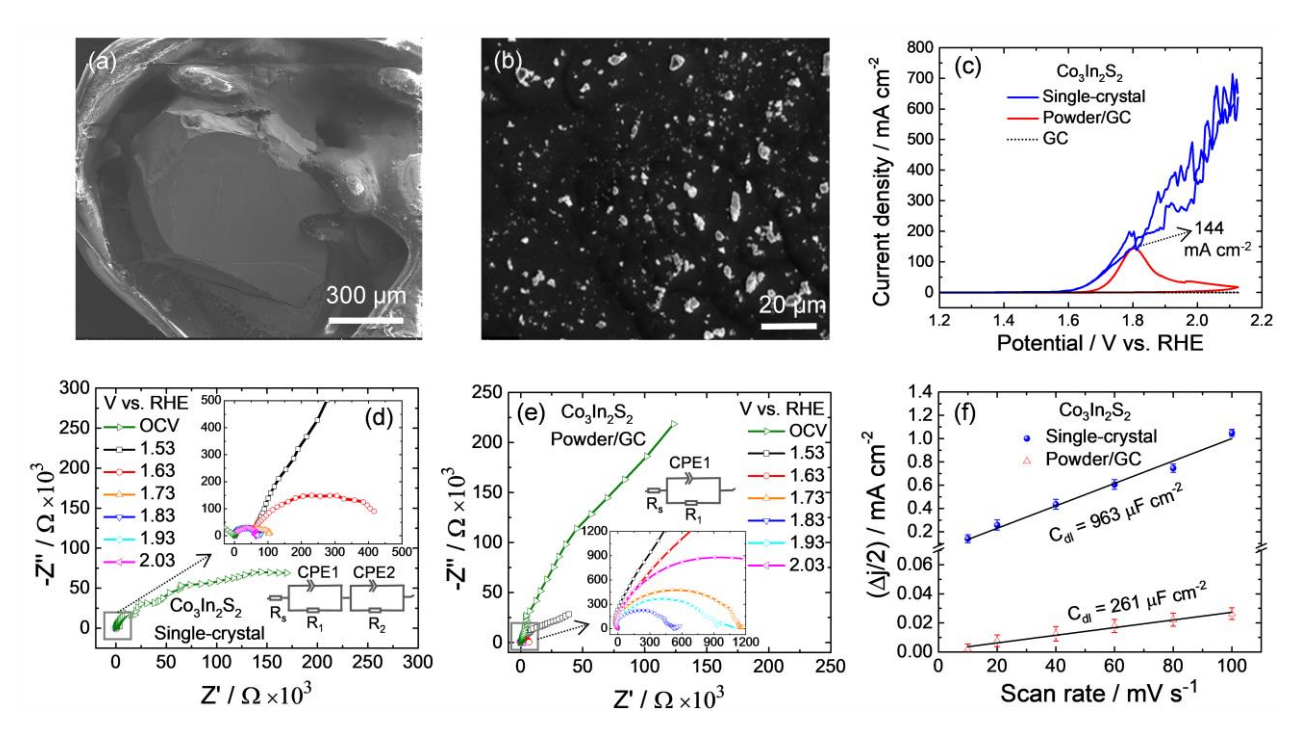


Fig. 1 Comparison of the morphological features and electrochemical activities of single-crystal $Co_3ln_2S_2$ and its powder. (a) and (b) The SEM images of single-crystal $Co_3ln_2S_2$ and its powder deposited on GC, respectively. (c) Oxygen evolution polarization curves of $Co_3ln_2S_2$ single-crystal, its powder on glassy carbon (Powder/GC) and bare GC. (d) and (e) The EIS plots of the $Co_3ln_2S_2$ crystal and its powder at various overpotentials, respectively. (f) The comparison of C_{dl} of $Co_3ln_2S_2$ single-crystal and Powder/GC electrodes.

and bare GC electrodes were recorded in the potential regime of 1.00-2.13 V vs. RHE (Fig. 1(c)). Contrary to the expectation, the powdered $\text{Co}_3\text{ln}_2\text{S}_2$ exhibited a 50 mV higher overpotential compared to its single-crystal counterpart at 100 mA cm^{-2} . The O_2 -gas bubbles were observed to stick to the particles on the Powder/GC electrode that act as a barrier layer to obstruct the availability of new sites for subsequent OER. Consequently, its OER polarization curve exhibits a distinctive mass-limited (bell-shaped) feature. Most likely, the defect-rich surface of powder particles could enhance its hydrophobic nature and reduce the interaction of H_2O and $\text{OH}^-.3^4$ Therefore, O_2 -gas bubbles adhere to the surface, lowering the OER current densities at higher overpotentials.

The Nyquist plots, obtained from the EIS of single-crystal $\text{Co}_3\text{In}_2\text{S}_2$ and powder/GC are displayed in Fig. 1(d) and (e), respectively. At open circuit voltage (OCV), neither of them developed a distinct semicircle. The single-crystal $\text{Co}_3\text{In}_2\text{S}_2$ exhibited a semicircle at potentials of 1.53 V vs. RHE and above. This semicircle appeared at the medium-high to high-frequency region (10^2-10^5 Hz) and was strongly independent of OER overpotential with a constant charge-transfer resistance (R_{ct}) of 55 Ω . Another interesting feature is that this semicircle appeared at a potential lower than the onset of OER (i.e., in the non-faradaic region), which suggests a phenomenon distinct from, and not related to OER kinetics. Furthermore, the absence of this semicircle at OCV implies its potential sensitivity (not

potential dependence). At 1.63 V vs. RHE, a potential greater than OER onset (1.60 V vs. RHE), a second semicircle emerged at lower frequencies (> 10² Hz) pertaining to OER kinetics. The EIS data is fitted to a two-time constant serial model circuit (inset Fig. 1(d)). Notably, the diameter of the second semicircle diminished rapidly with increased applied overpotential, reflecting an increase in the OER kinetics. Whereas the powder/GC showed only one semicircle in the whole frequency region (10⁻¹–10⁵ Hz) with a typical potential dependency from 1.53 to 2.13 V vs. RHE. The potential independent highfrequency semicircle has been commonly observed on bimetallic electrodes and it increases proportionally with the increase in surface inhomogeneities such as roughness (i.e., surface pores and surface oxide/hydroxide species).35-38 A similar potential independent semicircle was also observed on large-size single-crystals of delaffosite PdCoO₂ (3.44 × 10⁷ S m⁻¹ at 300 K, highest conductive oxide known), 25, 39 and CoS₂ (3.84 × 10⁵ S m⁻¹ at 300 K)²⁶ in alkaline OER, which was attributed to the fast electron transfer from the bulk of the single-crystal to its surface oxide layer. The topological materials hold high carrier mobility (μ) due to the linear electronic band dispersions. The electronic conductivity, σ ($\sigma = ne\mu$, where n is the carrier density and e is the charge of an electron i.e., 1.602 $\times 10^{-19}$ C) of topological semimetals Co₃Sn₂S₂,²⁴ Co₃In₂S₂,³¹ and Ni₃In₂S₂⁴⁰ are reported to be 3.8×10^{5} , 3.3×10^{5} and 4.0×10^{6} S m⁻¹ at 300 K, respectively. Owing to the excellent electronic conductivity of single-crystal Co₃In₂S₂, which originated due to the topology of

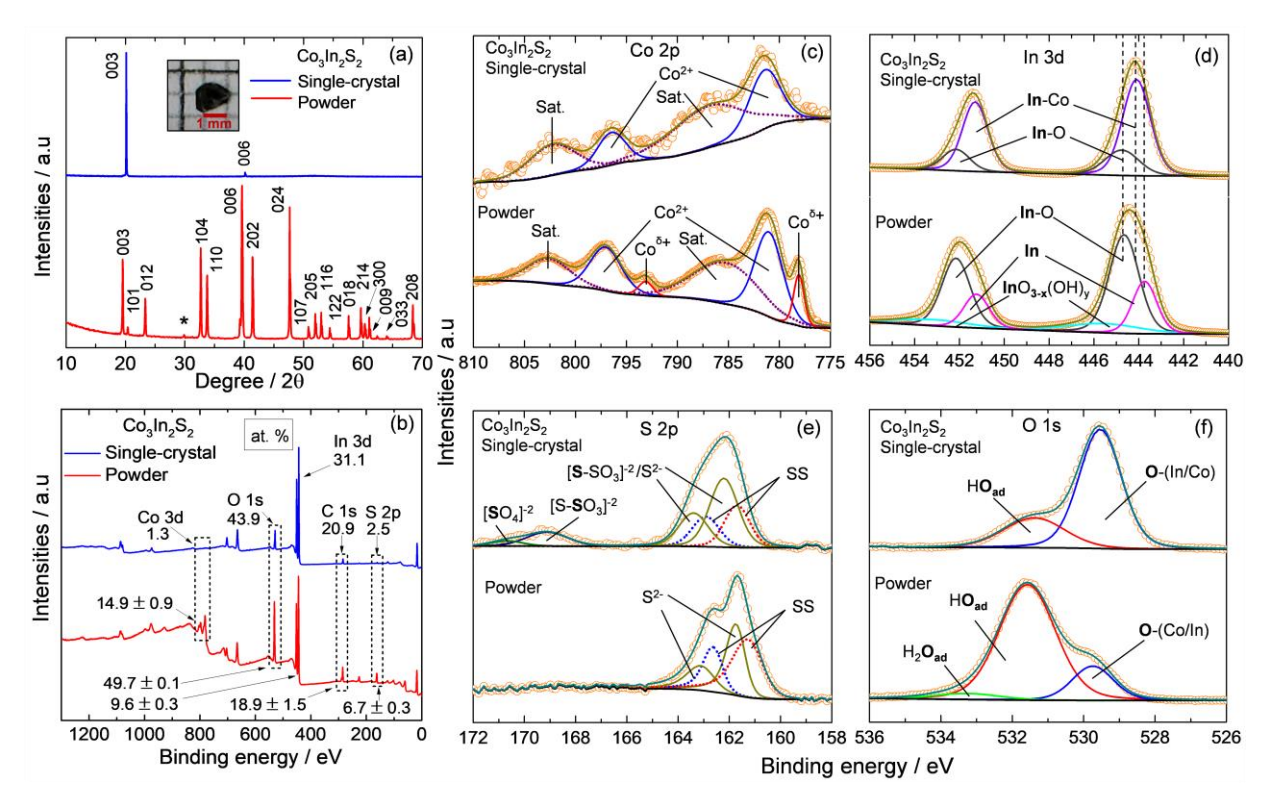


Fig. 2 Ambient grinding induced surface passivation of $Co_3ln_2S_2$. (a) The XRD patterns of single-crystal and powder $Co_3ln_2S_2$ with assigned crystal planes. (b) Compares the XPS survey spectra of single-crystal and powder $Co_3ln_2S_2$ in terms of surface atomic percentages. (c), (d), (e) and (f) Compares the XPS narrow spectra of Co 2p, In 3d, S 2p and O 1s $Co_3ln_2S_2$ (upper panel: single-crystal $Co_3ln_2S_2$; lower panel: powder $Co_3ln_2S_2$), respectively. (orange circles: raw data)

electronic bands, the electron transfer experiences a low scattering barrier between the $\text{Co}_3\text{In}_2\text{S}_2$ and thin surface In/Co-oxide layer. Hence, the potential independent semicircle appeared irrespective of OER in a relatively higher frequency region.

The double-layer capacitance (C_{dl}) of an electrocatalyst is proportional to its electrochemical active surface area (EASA), which reflects the fraction of active electrode/electrolyte interface that channels the charge. $^{41-43}$ To find the C_{dl} , the double-layer charging current density (j) of both single-crystal Co₃In₂S₂ and Powder/GC electrodes were measured at a series of scan rates of 10, 20, 40, 60, 80, 100 and 120 mV s⁻¹ (Fig. S5(a) and (b)). The value of j was taken as the average of anode and cathode current densities $[(|j_{anode}| + |j_{cathode}|)/2 = \Delta j/2]$ of CVs recorded in the non-faradaic region. The C_{dl} of single-crystal $\text{Co}_3\text{In}_2\text{S}_2$ and Powder/GC was calculated to be 963 and 261 μF cm $^{-2}$, Fig. 1(f)), respectively. The powder/GC holds lower C_{dl} compared to that of the single-crystal electrode due to the loss of area that is electrochemically active. This result indicates that the loss of area that is electrochemically accessible of powder/GC Co₃In₂S₂ is responsible for its lower OER kinetics. The bell shape of the CV and low C_{dl} of powder/GC could be a potential consequence of defect-rich and electrochemically non-conductive surface oxide species on the surface of powder Co₃In₂S₂ particles.

To rationalize the lower OER kinetics of powder/GC, powder XRD and high-resolution XPS analyses were carried out on single-crystal Co₃In₂S₂ and its high-surface area powder counterpart. The single-crystal Co₃In₂S₂ exhibits well-defined reflections at 2θ values of 19.60° and 39.62°, corresponding to the (003), and (006) planes, respectively (Fig. 2(a)). The reflections in XRD of powder Co₃In₂S₂ were labeled using the hkl file obtained from Rietveld refinement. The XRD pattern of the powder Co₃In₂S₂ displayed two distinct intensity zones, one with high-intensity reflections, spanning 20 values from 0 to 47.63° (lattice spacing > 3.05 Å), and the second zone with a low-intensity feature, starting from 50.84° (lattice spacing < 1.93 Å) and beyond. Particularly, the majority of the highintensity reflections correspond to the members of {hk0} family. No reflections from {hkl} family were observed in the highintensity region, indicating the absence of respective facets. A small reflection at 30° ('*') was identified as a minor In₂O₃ phase (JCPDS# 06-0416). In the low-intensity regions, several highindex facets, including (107), (205), (116), (122), (018), (214), (300), (009), (033) and (208), were detected. In the singlecrystal, the (003) planes are susceptible to cleavage during the grinding process, due to their relatively large lattice spacing (4.55 Å), resulting in the formation of the $\{hk0\}$ family.

The surface composition and chemical functionalities of the as-synthesized single-crystal and powder Co₃ln₂S₂ were

identified and compared using an XPS analysis. The survey spectra of as-synthesized single-crystal and powder Co₃In₂S₂ confirmed the presence of Co, In, S and O elements (Fig. 2(b)). The carbon peak at 285.0 eV, could have been generated during the synthesis process due to the presence of organic impurities in the raw materials (most probably the Co powder). Among the Co, In and S elements, In occupied the major surface of singlecrystal Co₃ln₂S₂ with an atomic percentage (at. %) of 31.10, whereas the Co and S elements were found to be only 1.31 and 2.46 %, respectively. Conversely, the surface of powder Co₃In₂S₂ contains Co and S elements with 14.91 and 6.69 at. %, respectively, which are 11.4 and 2.7 times higher than those observed for the single-crystal surface. The powder consists of 9.58 at. % of In-atoms which is 3.2 times lower than the singlecrystal surface of Co₃In₂S₂. In both the single-crystal and powder $Co_3In_2S_2$, the XPS survey spectrum revealed O as the predominant element, constituting 43.86 and 49.72 at. %, respectively. The surface of the powder exhibited a higher presence of oxygen-based species which suggests a potential oxidation of the surface, resulting from the grinding process at ambient conditions (water vapor and oxygen). The grinding of well-grown crystals is a stochastic process of breaking relatively weak inter-layer forces. The enrichment of Co- and S-at. % on the powder surface suggests the plausible breaking of Co-In bonds (2.66 Å) during the grinding process. Such freshly exposed Co- and In-sites with unsaturated coordination are vulnerable to oxidation in ambient conditions. The increased increment of the O-at. % on the powder surface supports the improved interaction of oxygen-based species with the newly formed surface of powder Co₃In₂S₂. The EIS and XPS analyses indicate that the surface of single-crystal Co₃In₂S₂ consists of a relatively thin In-based native oxide layer, whereas the powder surface is covered with Co- and In-based oxide species. Note that the presence of In (31.1) and O (43.9) at. % element on the pristine single-crystal surface is far higher than the other constituent elements (Co and S), which could be due to the In₂O₃ deposits on the crystal surface. The X-ray fluorescence (XRF) data also revealed the excess amount of In (Co:In:S mole ratio found to be 3:4.4:1.82) further agrees with the second indium phase on the surface of Co₃In₂S₂ single-crystal.

To identify the chemical nature of surface functionalities, high-resolution XPS was carried out in the region of Co, In, S and O elements and presented in Fig. 2(c)-(f). For the single-crystal, the Co 2p spectra exhibited doublet peaks at 781.3 and 796.3 eV for $2p_{3/2}$ and $2p_{1/2}$, respectively, with corresponding satellites at 786.3 and 802.2 eV. These peaks are ascribed to a Co2+ oxidation state, indicative of surface oxidation or loss of coordination (S^{2-} vacancies).⁴⁴ For the powder $Co_3In_2S_2$, similar doublet peaks centered at binding energies (BEs) of 781.1 and 797.2 eV, with a spin-orbit separation of 16.1 eV were attributed to the existence of a high spin Co2+ state.45 Additionally, a sharp peak appeared at a slightly higher BE (778.3 eV) than metallic Co (778.1 eV), which indicates the presence of a partially oxidized Co (Co^{δ_+}). For the single-crystal, the In $3d_{5/2}$ peak was deconvoluted into two peaks centered at BEs of 444.8 and 444.1 eV and attributed to the In—O present in the native In₂O₃ layer and Co—In present in the bulk-crystal. In the case of powder, the In 3d spectra appeared with asymmetric peaks. Each of these peaks was deconvoluted into three peaks (Fig. 2(d)). The peaks centered at 444.7 and 443.7 eV for the $3d_{5/2}$ are consistent with the In-O bond related to the defective In₂O₃ (In³⁺) and the metallic In (In⁰), respectively.⁴⁶ A tiny third peak fitted at BEs of 445.6 eV can be attributed to $In_2O_{3-x}(OH)_y$. ⁴⁷ The broad asymmetric O 1s core level spectra of single-crystal and powder $Co_3In_2S_2$ were deconvoluted into two and three peaks, respectively, as shown in Fig. 2(f). The lower BE peak at 529.1 eV is attributed to the lattice oxygen (O_{lat}). The higher BE peaks around 531.4 and 533.2 eV were consistent with the adsorbed hydroxyl (OHad) species and water (H2Oad) molecules onto the defect sites which could have been generated during the grinding of Co₃In₂S₂ single-crystals. The spontaneous dissociative adsorption of environmental water vapor on defect sites could lead to the hydroxylation of the crystal surface. The area under these peaks was calculated and attributed to their relative amounts present on the surface. The OH_{ad}/O_{lat} ratio increased after grinding the single-crystal Co₃In₂S₂ to powder from 0.37 to 4.06, indicating the enhancement in OH_{ad} species on the powder. The S 2p spectrum of single-crystal Co₃In₂S₂ was deconvoluted into four peaks. The BEs at 161.69, and 162.95 eV correspond to S²⁻ configuration, and 162.21 and 163.43 eV were associated with the surface derived states. The single-crystal Co₃In₂S₂ exhibited two minor peaks related to sulphate (SO_4^{2-}) and sulphite ($S_2O_3^{2-}$) species at BEs of 170.69 and 169.13 eV, respectively, which were absent on the powder surface. The high-resolution XPS analysis implies that the surface of single-crystal Co₃In₂S₂ occupied by the In₂O₃ surface layer with a minor phase of In₂O_{3-x}(OH)_y. Overall, the initial Co⁰—In²⁺ bond within the single-crystal Co₃In₂S₂ was disrupted during ambient grinding, leading to the disproportionation of In^{2+} into In^{3+} (i.e., $In_2O_3/In_2O_{3-x}(OH)_y$) and In⁰. Considering the increased at. % of Co^{2+} , $In_2O_{3-x}(OH)_y$ and OH_{ad} species, it can be concluded that the powder Co₃In₂S₂ surface is covered with In, Co(OH)₂ and In₂O_{3-x}(OH)_y species. The surface oxidation (*n*-type doping) can inject heavy electrons into the surface and annihilate the electron-transport properties of topological materials.48,49 Therefore, the surface of powder Co₃In₂S₂, covered with a heavy oxide/hydroxyl layer, decreases electrical conductivity and lowers the the electrode/electrolyte contact area. Furthermore, the rough morphology with increased defects and lowered crystallinity, promotes the hydrophobic nature of the powder surface, trapping the oxygen molecules and consequently impeding the OER by blocking the active surface.³⁴ The selenium vacancies and the formation of a surface oxide layer (~0.38 nm) are known to induce the trivial SS on Bi_2Se_3 nanoribbons and incorporate low-mobility charge carriers onto the surface. Consequently, the net effect of surface states and topological states has been reflected in the diminished electronic conductivity properties of Bi₂Se₃ nanoribbons.⁴⁹

2.3 Inactivity of surface Co-oxide/(oxy)hydroxides in $\text{Co}_3\text{In}_2\text{S}_2$ for OER. Electrocatalytic reactions are known to occur on the surface of electrocatalysts. The surface atoms in transition-

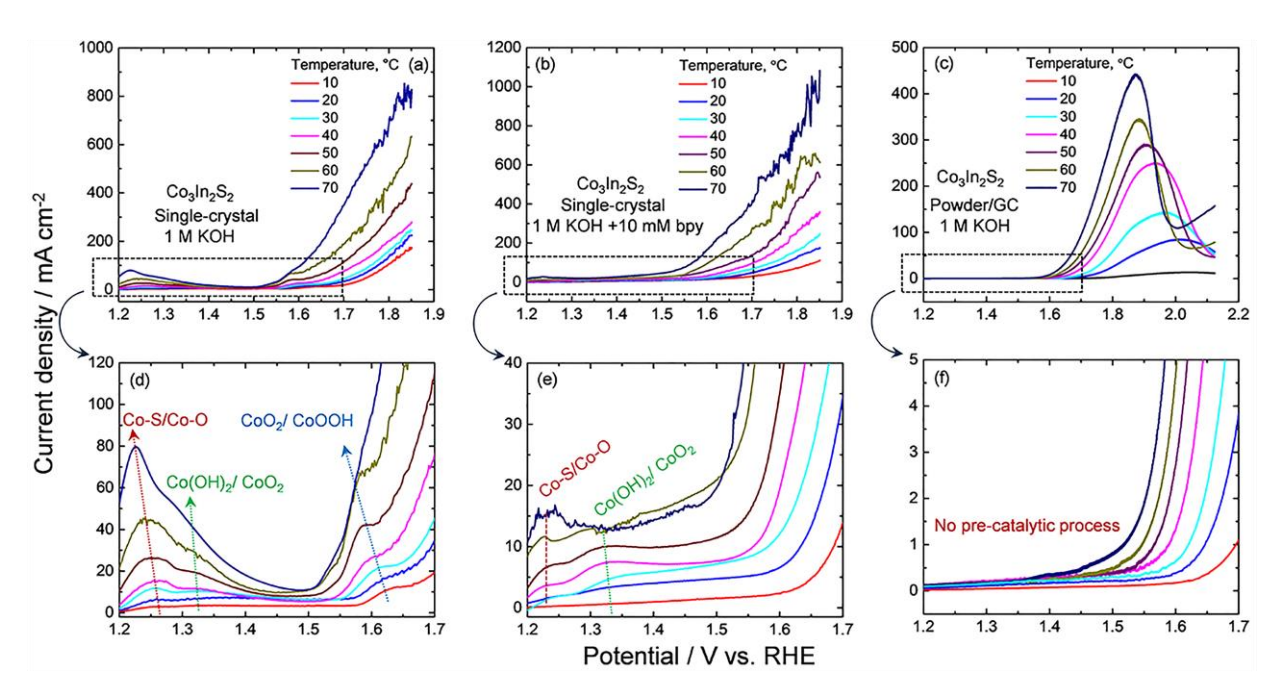


Fig. 3 Evolution of pre-catalytic redox peaks of Co-sites in $Co_3In_2S_2$ with temperature in 1 M KOH. Oxygen evolution polarization curves of $Co_3In_2S_2$ (a) and (b) single-crystal with and without 10 mM bpy in 1 M KOH at 10, 20, 30, 40, 50, 60 and 70 °C, scan rate of 10 mV s⁻¹, respectively, (c) Powder/GC (without *iR*-correction). (d) The pre-catalytic processes show the O-substitution followed by cobalt oxidation peaks. (e) The coordination of bpy ligands to Co-sites significantly reduced the cobalt oxidation peaks. (f) No pre-catalytic processes appeared for the Powder/GC due to the heavy surface oxide and defects.

metal-sulfides tend to undergo oxidation at high positive potentials (>1.0 V vs. RHE) owing to their relatively reactive nature.7 Consequently, the electrochemically oxidized species, such as metal oxides/(oxy)hydroxides were found to be the active sites due to their most structure/phase/crystallinity for the OER.50-52 To identify the possible oxidized active species on the surface of Co₃In₂S₂, a series of temperature-dependent CVs (for clarity only forward profiles were shown) were monitored on single-crystal Co₃In₂S₂ (in both 1 M KOH and 10 mM bpy + 1 M KOH) and Powder/GC (1 M KOH). The temperature range varied from 10 to 70 $^{\circ}$ C, with intervals of 10 °C (Fig. 3(a)-(f)). For single-crystal Co₃In₂S₂ in 1 M KOH at 10 °C, three small and broad oxidation peaks were observed at ~1.26, ~1.31 and ~ 1.62 V vs. RHE (pre-catalytic region) and concomitantly OER commenced. With an increase in the electrolyte temperature from 10 to 70 °C, the intensity of all oxidation peaks and OER current densities enhanced as shown in Fig. 3(a) and (d). The peak observed at 1.26 V vs. RHE was attributed to the incorporation of electrolyte oxygen in place of surface sulfur atoms within the Co-coordination sphere. 53 The peaks at $^{\sim}1.31$ and $^{\sim}1.62$ V vs. RHE were assigned to the conversion of $Co(OH)_2$ to CoO_2 and CoO_2 to CoOOH, respectively.54 The broad peaks that appeared at 1.26 and 1.62 V vs. RHE gradually shifted toward more negative potentials and also altered into a sharper feature with increasing temperatures. This alteration in the peak at 1.26 vs. RHE represents the faster kinetics of O-substitution due to the increased kinetic energy of oxygen in the electrolyte at higher temperatures. Recently, operando experiments on β -Co(OH)₂ revealed that the conversion of CoO₂ to CoOOH is facilitated by the deintercalation of water molecules from the layers through the edges.55 This deintercalation process becomes kinetically favorable with increasing temperature and accelerates the formation of CoOOH altering the peak at 1.62 V vs. RHE. The oxidation peak at 1.31 V vs. RHE does not shift significantly, which indicates the surface confined diffusionless process. To investigate the role of these pre-catalytic Co-species in OER kinetics, the surface Co-sites were blocked/poisoned with a well-known 'bpy' ligand. 56 The π-conjugated organic ligands such as bpy are known to strongly coordinate to the metal sites without intercalating into the bulk.⁵⁷ The OER polarization curves were collected using the single-crystal Co₃In₂S₂ electrode after immersing the electrode in a homogeneous electrolyte mixture of 10 mM bpy + 1 M KOH for 10 minutes. The precatalytic redox peaks were significantly suppressed at all the temperatures, as shown in Fig. 3(d) and (e), suggesting the complexation of Co-sites with bpy ligands. The OER activity slightly decreased after the blocking of the Co-sites and continued without any further decay. At lower temperatures (10–40 °C), the electrode did not show much improvement in the current density in 1 M KOH electrolyte as compared to 1 M KOH + 10 mM bpy electrolyte. These results not only indicate that the surface Co-based oxide/(oxy)hydroxide species (Co(OH)₂/CoO₂/CoOOH) are not the primary active sites but also the surface poison tolerant OER activity of single-crystal Co₃In₂S₂. It has been reported that the In⁺/In²⁺-bpy complex formation is unfavorable.58 Therefore, most likely, In-based sites are the OER active sites (further investigations discussed

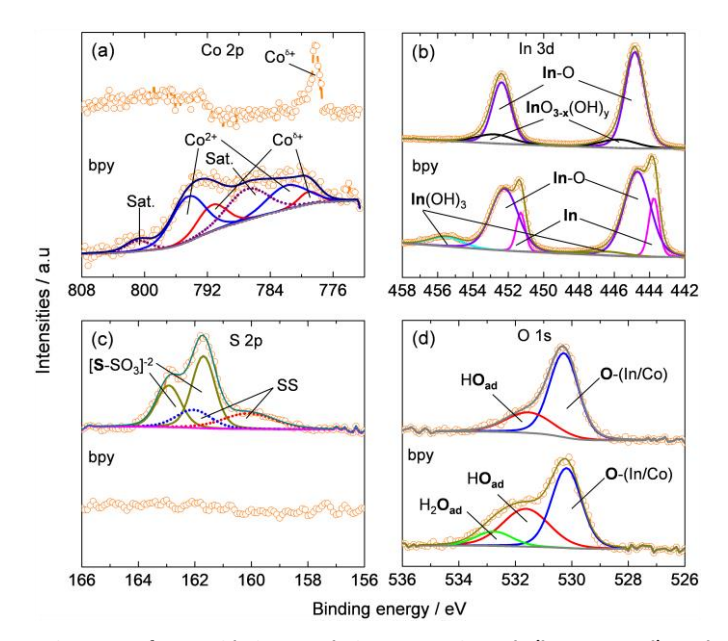


Fig. 4 Surface oxidation evolution on poisoned (lower panel) and unpoisoned (upper panel) single-crystal $Co_3In_2S_2$ electrodes: The XPS data of (a) Co 2p, (b) In 3d, (c) S 2p and (d) O 1s of bpy poisoned (1 M KOH + 10 mM bpy electrolyte) and unpoisoned (1 M KOH electrolyte) single-crystal $Co_3In_2S_2$ electrodes after a series of cyclic voltammograms in OER region at 10, 20, 30, 40, 50, 60 and 70 °C, scan rate of 10 mV s⁻¹.

under 'computation details'). The OER polarization curves of the Powder/GC electrode did not show any pre-catalytic peaks and the bell-shaped feature continued to appear at higher temperatures. As shown in Fig. 3(c), the bell-shape feature continues to appear in all the curves that are obtained at various temperatures (10–70 °C). This observation supports the claim

that the blockage of active surface area by O_2 bubble formation is potentially a more dominant factor over the hydrophobic nature of surface, resulting in the bell-shaped feature observed in Figure 1(c) and 3(c).

The XPS analysis was performed on both electrodes after a series of OER tests conducted over a temperature range of 10 to 70 °C (Fig. 4(a)-(d)). The electrode used in 1 M KOH electrolyte shows a distinct and intense peak corresponding to metallic Co particles was observed at 778.2 eV, indicating the presence of Co in its metallic state. Notably, no discernible signature of the Co^{2+} (Co $2p_{1/2}$ and $2p_{3/2}$ at 781.4 and 794.4 eV, respectively) state was detected on the surface of this electrode. Analysis of the In 3d spectra revealed two distinct peaks, which were attributed to In-O bonding in In₂O₃ (444.8 eV) and In₂O_{3-x}(OH)_y (445.9 eV), respectively. The coordination of bpy ligands from the 1 M KOH + 10 mM bpy electrolyte with the Co-sites appeared to stabilize the Co-sites on the electrode surface, leading to the disproportionation of In₂O₃, In(OH)₃, and partially oxidized metallic-In (Ind+) species. Examining the O 1s spectra revealed the presence of two distinct peaks: the Olat peak at 530.2 eV and the OH_{ad} peak at 531.6 eV, confirming the existence of In₂O_{3-x}(OH)_y. Additionally, a minor peak at 532.7 eV was attributed to H2Oad species. Notably, there was no discernible signature of S-states on the bpy-poisoned electrode, indicating the complete removal of sulphur from the lattice. Conversely, analysis of the S 2p of the unpoisoned electrode revealed two possible species: SS and S₂O₃-2. The bpy coordination-induced Co-site poisoning resulted in the complete oxidation of In sites from $In_2O_{3-x}(OH)_y$ to $In(OH)_3$, along with the removal of lattice sulphur. This phenomenon could be the potential reason for decrease in the OER current density observed in the case of the poisoned electrodes.

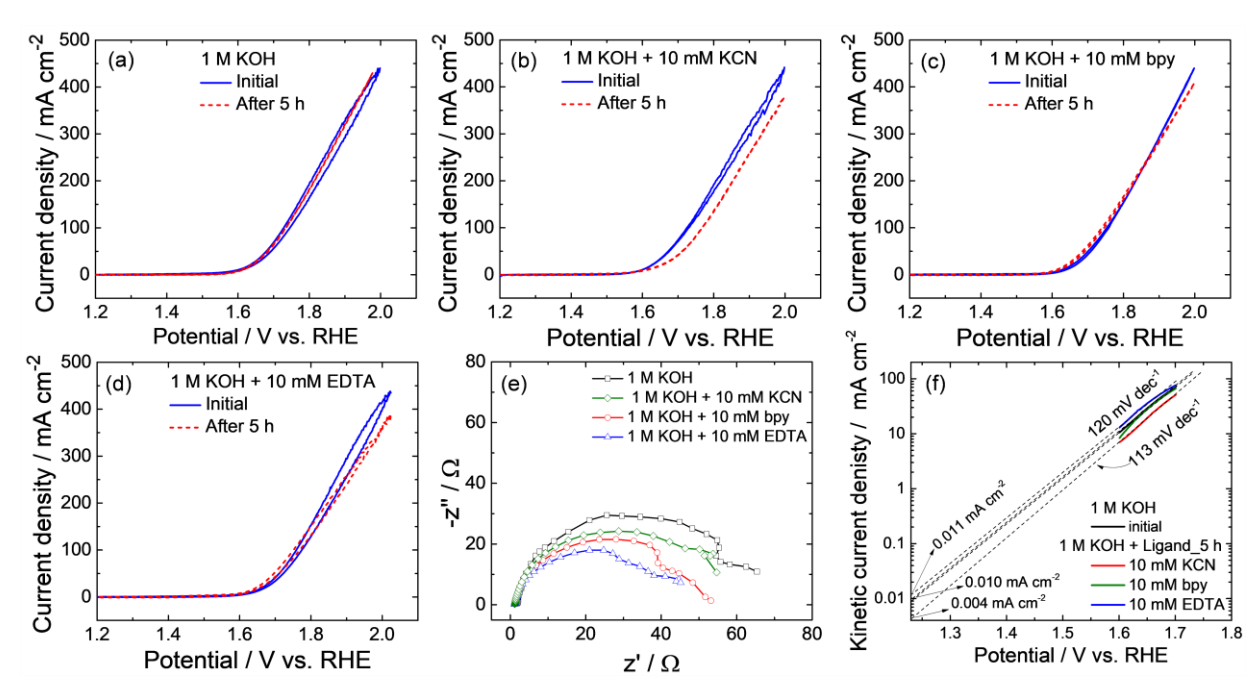


Fig. 5 Strong surface poison tolerance OER activity of single-crystal Co₃ln₂S₂. (a)-(e) show the CVs of initial and after 5 h OER activity of pristine and poisoned single-crystal Co₃ln₂S₂ with bpy, EDTA, and KCN. (f) Shows their respective EIS spectra after 5 h of OER activity.

2.4 Surface poison tolerance OER activity of Co₃In₂S₂. To further confirm the poison-tolerant OER activity of single-crystal Co₃In₂S₂, the electrodes were separately subjected to CV cycling for 5 h in 1 M KOH + 10 mM KCN, 1 M KOH + 10 mM bpy, and 1 M KOH + 10 mM EDTA. After immersing the single-crystal Co₃In₂S₂ in the respective electrolyte for 10 minutes, each electrode was subjected to 100 CV cycles (~ 5 h) at a scan rate of 10 mV s⁻¹. It was exciting to find that the OER activity of single-crystal $Co_3In_2S_2$ electrodes was retained without any significant decay. The initial and final OER polarization curves of pristine and poisoned (KCN, bpy, and EDTA) single-crystal Co₃In₂S₂ are presented in Fig. 5(a)-(d). An increment of only ~37 mV in the overpotential at 100 mA cm⁻² was observed on the KCN-poisoned single-crystal of Co₃In₂S₂, indicating its unique poison-tolerant activity compared to any known electrocatalysts so far. EIS experiments were carried out after poisoning the electrodes to understand the modifications in the charge transfer processes. The R_{ct} values were obtained from simplified Randles circuit fitting to the EIS data presented in Fig. 5(e). The simplified Randles circuit is an equivalent electrical circuit, which consists of solution resistance (R_s) in series to the parallel combination of the C_{dl} or constant phase element (CPE) and R_{ct}. The R_{ct} associated with the semicircle was obtained to be 69 Ω for pristine single-crystal Co₃In₂S₂, and 57, 55, 48 Ω for single-crystals poisoned with KCN, bpy, and EDTA at 1.83 V vs. RHE, respectively. The electrodes subjected to surface poisoning demonstrated a smaller diameter in the highfrequency semicircle compared to that of the pristine electrode. This decrease suggests lowered surface inhomogeneity, i.e., the surface roughness of the electrode. The iR-corrected CVs (R_s = 1.5 Ω) of the pristine (initial) and poisoned Co₃In₂S₂ (after 5 h of OER activity) were converted to Tafel plots. The Tafel slopes were determined to be 120 mV dec⁻¹ for pristine single-crystal,

as well as for the bpy-, and EDTA-poisoned single-crystal. The Tafel slope of KCN-poisoned single-crystal $Co_3In_2S_2$ was found to be 113 mV dec⁻¹. Although the OER overpotential for KCN-poisoned electrode increased while CV cycling, the Tafel slope suggests no significant change in the OER electron transfer mechanism. The calculated exchange current densities were 0.010 mA cm⁻² for pristine single-crystal $Co_3In_2S_2$ and 0.004, 0.010, and 0.011 mA cm⁻² for KCN-, bpy-, and EDTA-poisoned single-crystal $Co_3In_2S_2$, respectively.

After the poison tolerance test, electrodes were subjected to XPS analysis to investigate the surface chemical modifications. The high-resolution XPS spectra of Co 2p and In 3d and ligand atoms (C in CN-ligand, and N in bpy and EDTA) of the poisoned crystals are shown in Fig. 6(a)-(d). The BEs at 781.7 eV for $Co^{2+} 2p_{3/2}$ on both KCN- and bpy-poisoned single-crystal Co₃In₂S₂ surfaces exhibited a 0.4 eV shift to the higher BE as compared to the pristine single-crystal Co₃In₂S₂, indicating the strong coordination of KCN and bpy ligands to the Co²⁺-site. Additionally, the peaks at 778.7 and 778.6 eV imply the presence of partially oxidized Co ($Co^{\delta+}$). The KCN-poisoned single-crystal surface shows the highest intensity peak of $Co^{\delta+}$ species at 778.7 eV, which indicates the strong surface modification/defect formation due to the CN- ligand. The asymmetric In 3d doublet peaks of CN-poisoned single-crystal Co₃In₂S₂ were deconvoluted into two peaks. The BEs of 443.5 and 444.6 eV for 3d_{5/2}, suggest the existence of metallic In and In—O bond in defective In_2O_3 i.e., $In_2O_{3-x}(OH)_y$, respectively. Similarly, the slightly asymmetric In $3d_{5/2}$ (and $3d_{3/2}$) peak of bpy-poisoned single-crystal Co₃In₂S₂ was deconvoluted into two peaks centered at 443.8 and 444.7 eV, indicating partially oxidized metallic-In ($In^{\delta+}$) and $In_2O_{3-x}(OH)_y$. The EDTA-poisoned electrode did not display either metallic Co or In signatures. The

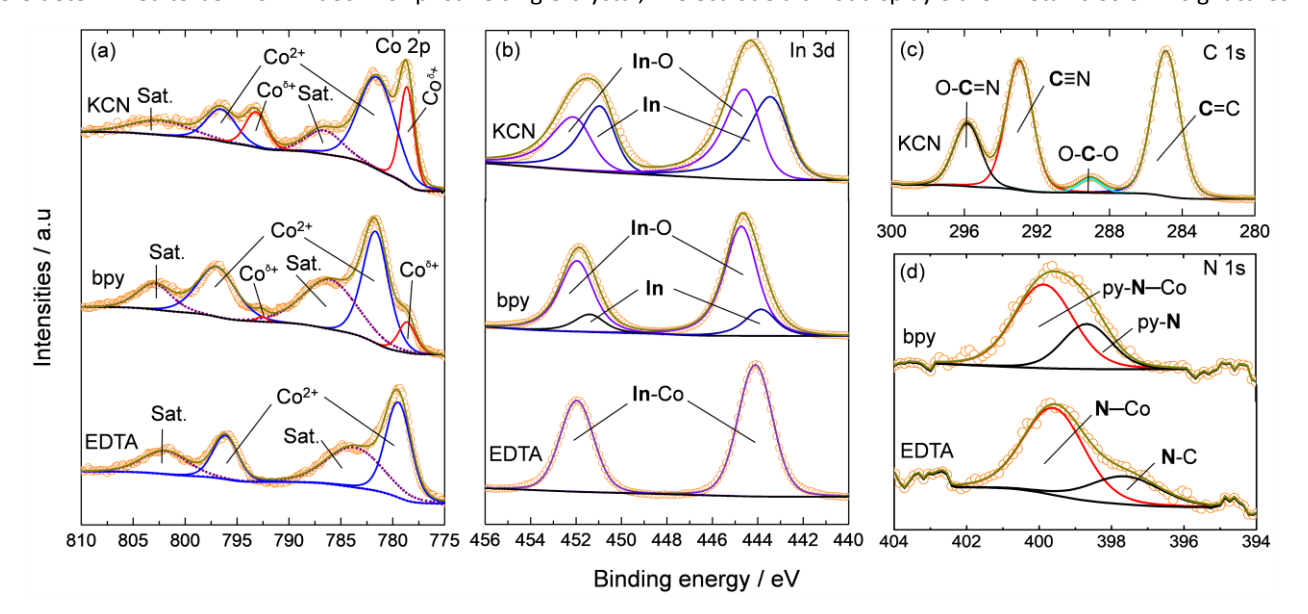


Fig. 6 High-resolution XPS of (a) Co 2p and (b) In 3d spectra for KCN-(top), bpy-(middle) and EDTA-poisoned (bottom) Co₃In₂S₂ electrodes, respectively. (c) XPS C 1s spectra for KCN-poisoned Co₃In₂S₂. (d) XPS N 1s spectra for bpy- and EDTA poisoned Co₃In₂S₂. (orange circles: raw data)

BE of 779.6 eV for Co $2p_{3/2}$, indicates the weak coordination of EDTA to Co^{2+} . The In $3d_{5/2}$ spectra exhibited a symmetric peak centered at 444.1 eV, indicating the presence of a Co-In/In-O bond, similar to pristine single-crystal Co₃In₂S₂ (bottom panel of Fig. 6(b)). We noticed that the strong coordination of ligands (KCN and bpy) to the Co-site, induced the In disproportionation reaction leading to the rupture of the Co—In bond, forming In3+ (In₂O_{3-x}(OH)_y) and In⁰ species. In the N 1s spectrum, the BEs of 398.7 and 399.9 eV were attributed to pyridinic-N (py-N) coordinated to Co²⁺ ion and the physisorbed bpy, respectively (top panel in Fig. 6(d)). Similarly, the BEs of 397.6, and 399.5 eV were attributed to N—C bonding in adsorbed EDTA and weakly coordinated N to Co2+, respectively (lower panel in Fig. 6(d)). In the C 1s spectra, the BEs at 292.77 and 295.45 eV were identified as the C species present in CN- ligand and (O—C=N) that are coordinated to surface Co2+ ions (Fig. 6(c)). The (O-C=N) and (O—C—O) species could be the products of oxidation at high positive potentials.

After the poisoning tests, electrolytes were subjected to inductively coupled plasmon mass spectrometry (ICP-MS) to quantify the leached amount of Co- and In-ions. The concentration of Co/In was measured to be 3746/21, 158/261, $210/127 \,\mu g \,L^{-1}$ in the 1 M KOH + 10 mM KCN, 1 M KOH + 10 mM bpy, and 1 M KOH + 10 mM EDTA electrolytes, respectively. The reduced OER activity in 1 M KOH + 10 mM KCN electrolyte could be due to the degradation of crystal structure of $\text{Co}_3\text{In}_2\text{S}_2$ and dissolution of Co-species. The emergence of potential independent high-frequency semicircle in the EIS spectra and the identification of the $In_2O_{3-x}(OH)_y$ phase indicates the robust In₂O_{3-x}(OH)_v/Co₃In₂S₂ heterostructure as a new active phase on the Co₃In₂S₂ single-crystal electrode during OER. The In₂O₃ semiconductor supported on carbon cloth is known to be a poor OER catalyst.⁵⁹ However, the oxygen deficient In₂O₃ phase i.e., In₂O_{3-x}(OH)_v supported on a highly conductive support (Weyl semimetal Co₃In₂S₂) exhibited high OER activity, excellent durability and remarkable poison tolerance activity. 60

2.5 Durability tests. To assess the possible application of singlecrystal Co₃In₂S₂ electrodes in industrial-level water electrolysers, we have carried out long-term durability tests at high current density. Chronoamperometric tests were carried out starting from 10, 25, 50, 100, 200, 250 mA cm⁻² and back to 10 mA cm⁻² by holding at 10 h at each step (Fig. 7(a)). The singlecrystal Co₃In₂S₂ exhibited excellent stability and sharp response for all the tested current densities, revealing the high masstransport, electrochemical and mechanical robustness of such single-crystals at high positive potentials. The forward trace of CV obtained before and after the 70 h staircase chronoamperometry showed no significant change (Fig. 7(b)). Although the electrode surface of the single-crystal Co₃In₂S₂ after 70 h of the multicurrent test exhibited some degree of roughness, it remained generally smooth and shiny (Fig. S6(a)-(c)). Realizing the remarkable poison tolerance, as well as stable OER activity at higher current densities of the single-crystal Co₃In₂S₂ electrode, a long-term durability test was conducted for 1000 h at 100 mA cm⁻² (electrode area: 0.0039 cm²,

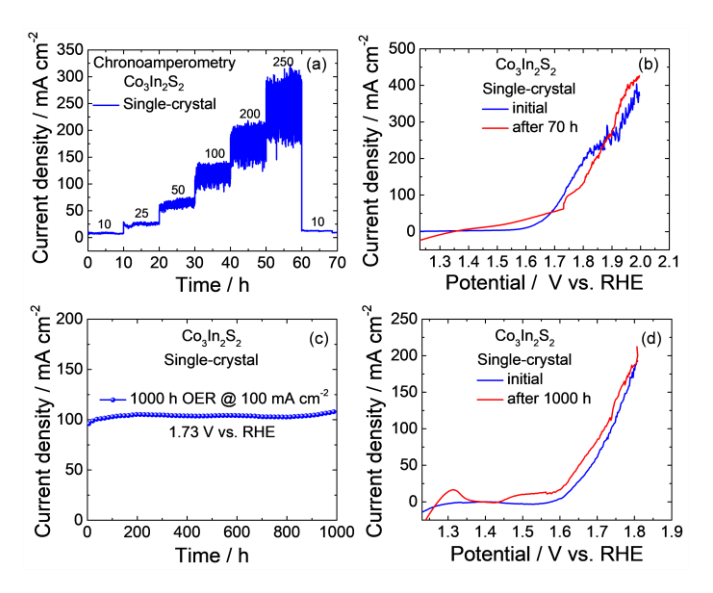


Fig. 7 Durability tests. (a) Multicurrent current process with the current density starting from 10 to 250 mA cm $^{-2}$ and back to 10 mA cm $^{-2}$, and (b) compares the OER polarization curves before and after multicurrent density test. (c) Chronoamperometric curve of single-crystal $Co_3In_2S_2$ at 100 mA cm $^{-2}$ and (d) compares the OER polarization curves before and after long-term durability test. (All the data presented here is without iR-correction)

thickness: 340 μ m, weight: 1.5 mg) in 1 M KOH electrolyte at 22 ± 2 °C. Every week 10 mL of fresh 1 M KOH was added to maintain the electrolyte amount during the durability test. The electrode exhibited excellent stability without decay in the OER activity over the operational duration of 1000 h (Fig. 7(c)). The morphology of the single-crystal electrode after 1000 h durability obtained using SEM showcases the highly inhomogeneous crystal surface covered with 1–3 μm of spheres and 5-7 μm of mossy-type spikes (Fig. S7(a)-(f)). The slight increase in the current density around 900 h could be the result of freshly opened edges as observed in the SEM image (Fig. S7(c)). The 18 mV lower overpotential observed after 1000 h for the single-crystal Co₃In₂S₂ electrode could be attributed to the increased surface area owing to the newly exposed edges. In addition to the single-crystal edges, the SEM image reveals the presence of dried silver paste. The exposed silver paste exhibited broad oxidation peaks at 1.3 V vs. RHE (Ag(OH)2 formation) and 1.5 V vs. RHE (Ag₂O formation), overlapping with the pre-catalytic Co-redox positions in Fig. 7(d).61 The amount of Co and In leached into the electrolyte was quantified using ICP-MS analysis. The quantity of Co and In leached into the electrolyte (100 mL) was 2.85 (0.190 wt. % of initial crystal) and 2.78 µg (0.185 wt. % of initial crystal), respectively, during the 1000 h durability test.

After the 1000 h durability test, the single-crystal $\text{Co}_3\text{In}_2\text{S}_2$ electrode was subjected to XPS analysis to understand the surface transformations (Fig. S8(a)-(d)). The high-resolution In $3d_{5/2}$ spectrum confirmed the presence of $\text{In}_2\text{O}_{3-x}(\text{OH})_y$ (444.6 eV) and metallic In state (443. 8 eV) (Fig. S8(a)). The BE of 455.7 eV could be the In–O bond present in the $\text{In}(\text{OH})_3$. The O 1s

spectrum features an intense peak associated with Olat (530.1 eV) and a slightly lower intense peak of HO_{ad} (532.1 eV), confirming the existence of In2O3-x(OH)y. Another lower intensity peak at 533.5 eV was attributed to H₂O_{ad} species. The Co 2p spectra lacked any resolvable peaks to identify its chemical state. No peaks relating to S 2p states were observed, which could be the result of complete O-substitution for the S2ions. The strong desulphurization Co₃In₂S₂ might form nonconductive species with hydrophobicity which caused the increased overpotential in the case of post-multi-current stability electrode OER profile.⁶² Overall, the surface of the single-crystal Co₃In₂S₂ appeared to be inhomogeneous, transforming primarily into In₂O_{3-x}(OH)_y as a stable and poison tolerant OER active phase with minor phases of In(OH)3, and metallic In. Although the In₂O₃ is a poor OER catalyst, the oxygen deficient In_2O_3 phase i.e., $In_2O_{3-x}(OH)_y$ formed on a highly conductive support (Weyl semimetal Co₃In₂S₂) exhibited high OER activity, excellent durability and remarkable poison tolerance activity. The lattice parameters of Rhombohedral In_2O_3 are a = b = 5.4814 Å and c = 14.4998 Å (space group: $R\overline{3}m$), which are slightly higher than the Co₃In₂S₂ crystal structure.63 However, the reduced bond lengths of the amorphous oxygen deficient In₂O₃ phase i.e., In₂O_{3-x}(OH)_y might be well-supported with less lattice strain (reduced In-O and In-In bond lengths) and improves the OER catalytic activity. 60, 64-67 Further, computational studies on the lattice strain effects of $Co_3In_2S_2/In_2O_{3-x}(OH)_y$ heterostructure on the OER activity are necessary to further improve the OER catalytic activity. Owing to the outstanding OER performance of single-crystal Co₃In₂S₂ with $In_2O_{3-x}(OH)_v$ surface layer, we have assembled water electrolyser (H-cell type) using the single-crystal Co₃In₂S₂ electrodes as a cathode as well as an anode as displayed in Fig. S9(a). The overall water splitting $(Co_3In_2S_2/In_2O_{3-x}(OH)_y)//(Co_3In_2S_2/In_2O_{3-x}(OH)_y)$ electrolyzer exhibited a cell voltage of 2.90 V at 500 mA cm⁻² (Fig. S9(b)). The cell showed a facile release of bubbles at both electrodes. The WE was carried out for 25 minutes and the generated oxygen and hydrogen gases were collected in the inverted measuring cylinders. The comparison of collected gas amounts with theoretical values revealed a faradaic efficiency of 100 %. (Fig. S9(c)).

2.6 Computational study. The DFT calculations were aimed to understand the OER mechanism at the surface of the catalyst. The adsorption of OER intermediates (e.g. HOO*, where * indicates the surface site) was calculated to understand the possible surface mechanism on In1, In2, Co and Co-In1 active sites. Initially, the surface facet was determined by finding the most favorable termination from (100), (110) and (111) facets and atom terminations (Fig. S13). The most favorable termination for the (110) facets was found to be a Co, In, and Sterminated surface. The adsorption energy of OOH* was calculated on four possible sites, i. In1-site, ii. In2-site, iii. Co-site and iv. The Co-In1 site was located as the most favorable OER site. All the sites resulted in positive adsorption energy values, which indicates that repulsive interaction of OOH occurs with these sites (Fig. S14). The order of the above-mentioned four

active sites is as follows, In2 (0.38 eV) < In1 (0.59 eV) ~ Co-In1 (0.60 eV) < Co (0.68 eV). Modeling the reaction pathway on the In 2 site indicates the facile conversion to OOH* as compared to the other adsorption sites. We therefore proceeded to calculate the Gibbs free energies for the reaction pathway at this site at a temperature of 293 K for the HO*, O* and HOO* intermediates on the In2-site. The resulting OER pathway is presented in Fig. 8(a). The limiting step in this pathway is the oxidation of HO* to O* which is endergonic with a reaction energy of 2.5 eV at an applied potential of -0.68 V. Although this is a high reaction energy and will be difficult to overcome at room temperature, the site is the most likely location for the reaction to take place as Co is known to be poisoned during the reaction and was not found to be present on the surface from the XPS spectra studies. The Co-In1 bridge site will not catalyze the oxidation reaction even though the site has a more favorable HO^* to O^* reaction energy (1.1 eV at -0.68 V) as shown in Fig. S15. A limitation of this model is the inability to model the $In_2O_{3-x}(OH)_y$ phase that occurs on the surface of Co₃In₂S₂ as it is an oxidized amorphous surface state. In order to define the surface state, different computation methods and more information about the formation of the amorphous state are necessary. The periodic nature of VASP does not lend itself to modelling amorphous interfaces because of the large unit cell

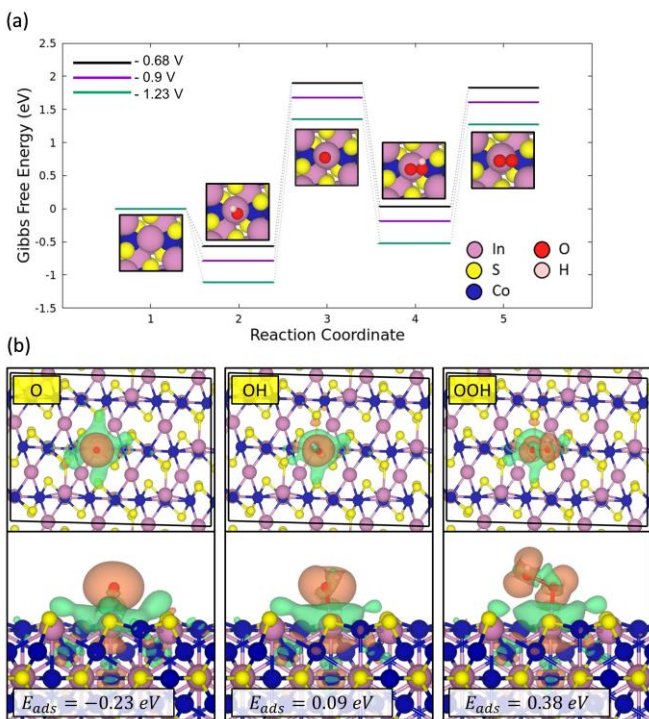


Fig. 8 Reaction Pathway. (a) The OER mechanism on the In2 bridge site by reaction coordinate vs. Gibbs Free Energy. The effects of a potential are shown by different line colors with values in the key at T=293 K. (b) Charge transfer calculations for the reaction intermediates for the OER on the In2 the surface gaining charge. The red areas indicate a charge loss while the green areas indicate a charge gain. The isosurface used is 0.005 eV/Bohr³.

sizes that would be required to model the amorphous surface which is not tractable at a DFT level of accuracy. Instead, we can investigate the interaction between O* and the Co₃In₂S₂ surface In. The high adsorption energy of O* in the Co-In1-site indicates that an O bridge could connect the $\text{Co}_3\text{In}_2\text{S}_2$ surface to the amorphous phase shown in Fig. S15 and this adsorption likely leads to poisoning of this active site. Additionally, OOH* in the In2-site has a low ΔG_{HOO^*} and is therefore more stable than both O* and OO* on the $\text{Co}_3\text{In}_2\text{S}_2$ surface. OH* and OOH* are stabilized on the surface due to the additional H as compared to the adsorbates without H involved (O* and OO*). A partial density of states is shown in Fig. S12 and shows that In loses states in its p-orbital below the Fermi level when adsorbates are present. While O* in all cases (Fig. S12(b)-(d)) have states around the Fermi level, this indicates that further adspecies will adsorb to the O on the surface and create an amorphous surface state. Overall, these results indicate that the Co₃In₂S₂ surface will not conduct the OER and the amorphous surface state is imperative to catalyze the reaction.

3. Experimental

- 3.1 Synthesis of Co₃In₂S₂ single-crystals. Single-crystals of Co₃In₂S₂ were synthesized by the chemical vapor transport technique with a slight modification to the reported procedure.24 The single crystals of Co₃In₂S₂ were prepared by mixing Co, In and S in the stoichiometric ratio (total amount 1 g) and sealed in an evacuated quartz tube (20 cm long) with ~5 mg of I₂ as a transport agent. The quartz tubes were then moved into a single-zone furnace and set to a temperate program as shown in Scheme S1. A heating rate of 0.33 °C minute⁻¹ to reach 1050 °C and 24 h of dwell time was applied to the sample. Then, a cooling rate of 3 °C h⁻¹ was applied to decrease the temperature to 600 °C followed by natural cooling to room temperature. The well-grown single-crystals of 1–1.5 mm size were collected and utilized further for structural and electrochemical characterizations. The total steps involved in the synthesis of Co₃In₂S₂ are shown in Scheme S1.
- **3.2 Electrode preparation.** Well-grown single-crystals of 1–1.5 mm in size were selected to prepare the electrodes for OER. As shown in Scheme S2, at first, the single-crystals were attached to 0.3 mm diameter and $^{\sim}$ 6 cm long copper wire using silver conductive paste followed by curing them at 70 °C for 5 h. In the next step, the hydrophobic Silicone glue was coated as an insulation layer and cured at 70 °C for 5 h.
- **3.3 Physical characterization.** Single-crystal X-ray diffraction (SC-XRD) was performed to obtain the lattice parameters. Powder XRD was conducted to confirm the phase purity of $\text{Co}_3\text{ln}_2\text{S}_2$. Rietveld refinement was carried out to obtain the lattice parameters and crystallographic information file. The $\text{Co}_3\text{ln}_2\text{S}_2$ crystalizes in R_3^{M} space group, Rhombohedral crystal system. The patterns of powder XRD and lattice parameters of SC-XRD are well-matched with the reported data. Scanning electron microscopy and energy-dispersive X-ray (EDS) analysis studies were conducted on FEI Apreo Volumescope with EDS

and EBSD detectors. The XRF data was obtained using Bruker S4 T-star analyzer. A 2 mg of Co $_3$ In $_2$ S $_2$ single-crystal was digested in 10 mL of concentrated (69-71 %) HNO $_3$ at 60 °C for 24 h. The final sample was composed of 100 μ L of the digested crystal solution, 10 μ L of 1000 μ g mL $^{-1}$ Gallium (standard element) and 890 μ L of water. A quartz disc with 10 μ L Serva solution (this siliconizes the disc and prevents liquid samples from spreading too far) used as a sample carrier. Finally, a 10 μ L of sample was pipette out on to the center of the quartz disc and dried under the heat lamp before subjecting to XRF analysis.

- **3.4.** X-ray photoelectron spectroscopy experimental description. X-ray Photoelectron Spectroscopy measurements were performed using a Thermo Fisher NEXSA spectrometer with a 125 mm mean radius, full 180° hemispherical analyzer, and 128-channel detector. This system uses a focused monochromatic Al K α X-ray (1486.7 eV) source for excitation and an electron emission angle of 60°. The narrow scan spectra were collected using a pass-energy of 50 eV with a step size of 0.1 eV. For the Ag $3d_{5/2}$ line, these conditions produced a full width at half maximum of 0.84 eV \pm 0.02 eV. The binding energy (BE) scale is calibrated using the Cu $2p_{3/2}$ feature at 932.62 \pm 0.05 eV and Au $4f_{7/2}$ at 83.96 \pm 0.05 eV. All the spectra were referenced to the aliphatic carbon at BE of 285.0 eV.
- **3.5 Electrochemical studies.** All electrochemical measurements were carried out using a three-electrode setup at 22 \pm 2 °C and 1 M KOH electrolyte. Co₃In₂S₂ single-crystal electrode as working electrode, Hg/HgO as reference electrode and 2 mm diameter graphite rod counter electrode. The potential applied against the reference electrodes was converted to a RHE using the equation, E (vs. RHE) = E (vs. Hg/HgO) + 0.105 V (E° (vs. Hg/HgO)) + 0.059pH.⁶⁸ A Gamry 600 potentiostat was used for all the electrochemical characterizations. Electrochemical impedance spectroscopy was carried out to extract the solution resistance, R_{ct} and diffusion resistance values. The obtained impedance data was fitted either to a two-time constant circuit or a simplified Randles circuit to extract the R_{ct} values.
- 3.6 Computation details. Theoretical calculations on the Co₃In₂S₂ surface were performed using Vienna Ab-Initio Software Package (VASP)^{69, 70} 6.1.2 using the planewave augmented wave method (PAW-PBE)⁷¹. The exchange correlation was calculated using the Perdue-Burke-Erzenholf (PBE) functional 72. Energy difference tolerance between SCF cycles was 1.0×10⁻⁴ eV and the force tolerance was 0.03 eVÅ⁻¹ with Gaussian smearing. Bulk optimizations were performed on the Kagome Lattice cell to calculate the lattice constant with a $6\times6\times2$ k-point mesh and a cell volume of 334.1 Å³ was found with a=b=5.322 Å and c=13.621 Å and $\alpha=\beta=90.0^\circ$ and $\gamma=10.0^\circ$ 120.0°. A corresponding cif file of the bulk structure is attached as supplementary information. An energy vs. volume curve is also shown in Fig. S10. We optimized the bulk with spin-orbit coupling as well as paramagnetic, finding the difference between them was minimal in band structure calculations. The paramagnetic surface was used for further calculation because there is increased computational efficiency as compared to

systems with spin-orbit coupling. The electronic state of the system at experimental conditions was confirmed to be paramagnetic, further justifying the model simplifications.

The band structure of the bulk $Co_3In_2S_2$ was obtained and presented in Fig. S11 where the Weyl points are highlighted. This structure was created with the aid of VASPKIT⁷³⁻⁷⁵ which created the proper k-space sampling coupled with the p4vasp software that interpreted the eigenvalue data for the distinctive bands. The appearance of these Weyl points indicates this material is a Weyl semimetal. Analyzing the electronic properties of the $Co_3In_2S_2$ of the surface gives further information on the material. In this regard, we show in Fig. S12, a partial density of states of the In and the corresponding shift of the DOS in the presence of adsorbates.

Surface optimizations were performed on a 2×2 surface with four layers with both the (110), (100) and (111) facet Cotermination. As shown in Fig. S13, the (111) facet termination 4 was the most favorable, but to accommodate the experimental work we chose to model the (110) facet termination 2 due to their availability in as-prepared crystals and the activity of (110). The cutoff energy for the surface calculations is 400 eV. The surface was converged using $2\times2\times1$ Gamma Point k-point mesh and a 12 Å vacuum with dipole corrections to ensure that the surfaces did not interact across periodic boundaries. The adsorption analysis was performed using the OOH intermediate on the various sites shown in Fig. S14.

4. Conclusions

In this work, we have synthesized mechanically stable and electrochemically robust single-crystals of Co₃In₂S₂ and employed them as ink-free and substrate-free electrodes for OER in 1 M KOH. The electrodes exhibited ultra-stable and an excellent durability of 1000 h at 100 mA cm⁻² without significant change in the overpotential. Remarkably, the OER activity was maintained in 10 mM of strong surface-poisoning ligands i.e., KCN, bpy, and EDTA containing 1 M KOH. The high-resolution XPS analysis and EIS spectra of pristine and poisoned singlecrystal Co₃In₂S₂ revealed the presence of In₂O₃ surface layer and the electrochemically formed In₂O_{3-x}(OH)_y during the OER. Thus formed $In_2O_{3-x}(OH)_y$ surface layer on the $Co_3In_2S_2$ $(Co_3In_2S_2/In_2O_{3-x}(OH)_y$ heterostructure) could be the origin of excellent stability and poison tolerance OER activity. This work paves the path for the development of poison-tolerant and high-performance electrocatalysts based $Co_3In_2S_2/In_2O_{3-x}(OH)_y$ for economical and industrial WE and other environmentally friendly energy conversion and storage devices such as fuel cells and rechargeable metal-air batteries.

Author contributions

Anjaiah Sheelam: Conceptualization, Methodology, Validation, Investigation, Visualization, Data curation, Writing- Original draft preparation. **Ariel Whitten:** Formal analysis, Investigation, Writing - Review & Editing. **Carrington Gates Moore:** Formal analysis,

Investigation, Writing- Review & Editing. Mark Engelhard: Investigation, Writing - Review & Editing. Jean-Sabin McEwen: Methodology, Writing- Review & Editing. Jeffrey G. Bell: Funding acquisition, Conceptualization, Supervision, Methodology, Writing-Review & Editing.

Conflicts of interest

There are no conflicts to declare.

Acknowledgements

A.W. acknowledges the financial support from the National Science Foundation Ceramics Program under DMR-1929306. C.M. and J.-S.M. acknowledge the financial support from the National Science Foundation CAREER program under CBET-1653561. This work was partially funded by the Joint Center for Deployment and Research in Earth Abundant Materials (JCDREAM) in Washington State. We also thank Dr. Dezhou Guo for the fruitful DFT discussions. Computational resources were provided by the Kamiak HPC under the Center for Institutional Research Computing at Washington State University. The Pacific Northwest National Laboratory is operated by Battelle for the U.S. DOE.

References

- H. Dau, C. Limberg, T. Reier, M. Risch, S. Roggan and P. Strasser, ChemCatChem, 2010, 2, 724-761.
- H. Jin, X. Wang, C. Tang, A. Vasileff, L. Li, A. Slattery and S. Qiao, Adv. Mater., 2021, 33, 2007508.
- J. Guo, Y. Zheng, Z. Hu, C. Zheng, J. Mao, K. Du, M. Jaroniec, S.-Z. Qiao and T. Ling, *Nat. Energy*, 2023, 8, 264-272.
- J. G. Vos, Z. Liu, F. D. Speck, N. Perini, W. Fu, S. Cherevko and M. T. M. Koper, ACS Catal., 2019, 9, 8561-8574.
- C. Liang, W. Pan, P. Zou, P. Liu, K. Liu, G. Zhao, H. J. Fan and C. Yang, Small, 2022, 18, 2203663.
- C. Dang Van, S. Kim, M. Kim and M. H. Lee, ACS Sustain. Chem. Eng., 2023, 11, 1333-1343.
- S. Niu, T. Tang, Y. Qu, Y. Chen, H. Luo, H. Pan, W.-J. Jiang, J. Zhang and J.-S. Hu, CCS Chemistry, 2023, 0, 1-12.
- C. Huang, Q. Zhou, D. Duan, L. Yu, W. Zhang, Z. Wang, J. Liu, B. Peng, P. An, J. Zhang, L. Li, J. Yu and Y. Yu, *Energy Environ. Sci.*, 2022, 15, 4647-4658.
- D. Li, W. Wan, Z. Wang, H. Wu, S. Wu, T. Jiang, G. Cai, C. Jiang and F. Ren, Adv. Energy Mater., 2022, 12, 2201913.
- Z. Yu, Y. Li, V. Martin-Diaconescu, L. Simonelli, J. Ruiz Esquius, I. Amorim, A. Araujo, L. Meng, J. L. Faria and L. Liu, Adv. Funct. Mater., 2022, 32, 2206138.
- 11. F.-L. Wang, N. Xu, C.-J. Yu, J.-Y. Xie, B. Dong, X.-Y. Zhang, Y.-W. Dong, Y.-L. Zhou and Y.-M. Chai, *Appl. Catal. B: Environ.*, 2023, **330**, 122633.
- W. Shen, Y. Zheng, Y. Hu, J. Jin, Y. Hou, N. Zhang, L. An, P.
 Xi and C.-H. Yan, J. Am. Chem. Soc., 2024, 146, 5324-5332.
- Y. Hou, M. Qiu, M. G. Kim, P. Liu, G. Nam, T. Zhang, X. Zhuang, B. Yang, J. Cho, M. Chen, C. Yuan, L. Lei and X. Feng, *Nat. Commun.*, 2019, **10**, 1392.

- M.-Y. Ye, S. Li, X. Zhao, N. V. Tarakina, C. Teutloff, W. Y. Chow, R. Bittl and A. Thomas, *Adv. Mater.*, 2020, 32, 1903942.
- 15. B. Chen, X. He, F. Yin, H. Wang, D.-J. Liu, R. Shi, J. Chen and H. Yin, *Adv. Funct. Mater.*, 2017, **27**, 1700795.
- K. Gong, F. Du, Z. Xia, M. Durstock and L. Dai, Science, 2009, 323, 760-764.
- D. Malko, T. Lopes, E. Symianakis and A. R. Kucernak, J. Mater. Chem. A, 2016, 4, 142-152.
- W. Yang, J. Li, L. Lan, Q. Fu, L. Zhang, X. Zhu and Q. Liao, Int. J. Hydrogen Energy, 2018, 43, 8474-8479.
- H. B. Yang, J. Miao, S.-F. Hung, J. Chen, H. B. Tao, X. Wang, L. Zhang, R. Chen, J. Gao, H. M. Chen, L. Dai and B. Liu, Sci. Adv., 2016, 2, e1501122.
- J. Zhang, Z. Zhao, Z. Xia and L. Dai, *Nat. Nanotechnol.*, 2015, 10, 444-452.
- M.-S. Balogun, W. Qiu, H. Yang, W. Fan, Y. Huang, P. Fang,
 G. Li, H. Ji and Y. Tong, *Energy Environ. Sci.*, 2016, 9, 3411-3416
- Z. Pei, H. Tan, J. Gu, L. Lu, X. Zeng, T. Zhang, C. Wang, L. Ding, P. J. Cullen, Z. Chen and S. Zhao, *Nat. Commun.*, 2023, 14, 818.
- 23. R. Wu and S.-H. Yu, Chem Catal., 2023, **3**, 100635.
- 24. G. Li, Q. Xu, W. Shi, C. Fu, L. Jiao, M. E. Kamminga, M. Yu, H. Tüysüz, N. Kumar, V. Süß, R. Saha, A. K. Srivastava, S. Wirth, G. Auffermann, J. Gooth, S. Parkin, Y. Sun, E. Liu and C. Felser, *Sci. Adv.*, **5**, eaaw9867.
- G. Li, S. Khim, C. S. Chang, C. Fu, N. Nandi, F. Li, Q. Yang, G.
 R. Blake, S. Parkin, G. Auffermann, Y. Sun, D. A. Muller, A.
 P. Mackenzie and C. Felser, ACS Energy Lett., 2019, 4, 2185-2191.
- 26. Y. Kang, Y. He, D. Pohl, B. Rellinghaus, D. Chen, M. Schmidt, V. Süß, Q. Mu, F. Li, Q. Yang, H. Chen, Y. Ma, G. Auffermann, G. Li and C. Felser, *ACS Appl. Mater. & Interfaces*, 2022, **14**, 19324-19331.
- Z. Wang, Z. Lin, Y. Wang, S. Shen, Q. Zhang, J. Wang and W. Zhong, *Adv. Mater.*, 2023, 35, 2302007.
- L. Wang, Y. Yang, J. Wang, W. Liu, Y. Liu, J. Gong, G. Liu, X.
 Wang, Z. Cheng and X. Zhang, *EcoMat*, 2023, 5, e12316.
- M. Lv, G. Yu and W. Chen, *Inorg. Chem. Front.*, 2022, 9, 6133-6146.
- D. W. Boukhvalov, G. D'Olimpio, F. Mazzola, C.-N. Kuo, S. Mardanya, J. Fujii, G. G. Politano, C. S. Lue, A. Agarwal, I. Vobornik, P. Torelli and A. Politano, *J. Phys. Chem. Lett.*, 2023, 14, 3069-3076.
- M. A. McGuire, Q. Zhang, H. Miao, W. Luo, M. Yoon, Y. Liu, T. Yilmaz and E. Vescovo, *Chem. Mater.*, 2021, 33, 9741-9749.
- P. Gütlich, K.-J. Range, C. Felser, C. Schultz-Münzenberg, W. Tremel, D. Walcher and M. Waldeck, *Angew. Chem. Int. Ed.*, 1999, 38, 2381-2384.
- W. Xu, D. Cao, O. A. Moses, B. Sheng, C. Wu, H. Shou, X.
 Wu, S. Chen and L. Song, *Nano Research*, 2021, **14**, 4534-4540.
- 34. G. Qi, X. Liu, C. Li, C. Wang and Z. Yuan, *Angew. Chem. Int. Ed.*, 2019, **58**, 17406-17411.
- 35. L. Chen and A. Lasia, J. Electrochem. Soc., 1992, 139, 3214.
- P. Los, A. Lasia, H. Ménard and L. Brossard, J. Electroanal. Chem., 1993, 360, 101-118.
- B. Børresen, G. Hagen and R. Tunold, *Electrochim. Acta*, 2002, 47, 1819-1827.

- 38. E. Navarro-Flores, Z. Chong and S. Omanovic, *J. Mol. Catal. A: Chem.*, 2005, **226**, 179-197.
- C. W. Hicks, A. S. Gibbs, A. P. Mackenzie, H. Takatsu, Y. Maeno and E. A. Yelland, *Phys. Rev. Lett.*, 2012, **109**, 116401.
- H. Fang, M. Lyu, H. Su, J. Yuan, Y. Li, L. Xu, S. Liu, L. Wei, X. Liu, H. Yang, Q. Yao, M. Wang, Y. Guo, W. Shi, Y. Chen, E. Liu and Z. Liu, Sci. China Mater., 2023, 66, 2032-2038.
- 41. J. O. M. Bockris and S. Srinivasan, *J. Electroanal. Chem.*, 1966, **11**, 350-389.
- R. Boggio, A. Carugati and S. Trasatti, J. Appl. Electrochem., 1987, 17, 828-840.
- 43. S. Trasatti and O. A. Petrii, *J. Electroanal. Chem.*, 1992, **327**, 353-376.
- N. S. McIntyre and M. G. Cook, Anal. Chem., 1975, 47, 2208-2213.
- 45. M. Oku and K. Hirokawa, *J. Electron. Spectrosc. Relat. Phenom.*, 1976, **8**, 475-481.
- 46. R. W. Hewitt and N. Winograd, *J. Appl. Phys.*, 2008, **51**, 2620-2624.
- L. B. Hoch, T. E. Wood, P. G. O'Brien, K. Liao, L. M. Reyes,
 C. A. Mims and G. A. Ozin, Adv. Sci., 2014, 1, 1400013.
- J. G. Analytis, J.-H. Chu, Y. Chen, F. Corredor, R. D. McDonald, Z. X. Shen and I. R. Fisher, *Phys. Rev. B*, 2010, 81, 205407.
- D. Kong, J. J. Cha, K. Lai, H. Peng, J. G. Analytis, S. Meister,
 Y. Chen, H.-J. Zhang, I. R. Fisher, Z.-X. Shen and Y. Cui, ACS
 Nano, 2011, 5, 4698-4703.
- H. Jiang, Q. He, X. Li, X. Su, Y. Zhang, S. Chen, S. Zhang, G. Zhang, J. Jiang, Y. Luo, P. M. Ajayan and L. Song, *Adv. Mater.*, 2019, **31**, 1805127.
- X. Liu, K. Ni, B. Wen, R. Guo, C. Niu, J. Meng, Q. Li, P. Wu,
 Y. Zhu, X. Wu and L. Mai, ACS Energy Lett., 2019, 4, 2585-2592.
- Y. Duan, S. Sun, Y. Sun, S. Xi, X. Chi, Q. Zhang, X. Ren, J. Wang, S. J. H. Ong, Y. Du, L. Gu, A. Grimaud and Z. J. Xu, Adv. Mater., 2019, 31, 1807898.
- Y. Hu, Y. Zheng, J. Jin, Y. Wang, Y. Peng, J. Yin, W. Shen, Y. Hou, L. Zhu, L. An, M. Lu, P. Xi and C.-H. Yan, *Nat. Commun.*, 2023, 14, 1949.
- J. T. Mefford, Z. Zhao, M. Bajdich and W. C. Chueh, *Energy Environ. Sci.*, 2020, 13, 622-634.
- J. T. Mefford, A. R. Akbashev, M. Kang, C. L. Bentley, W. E. Gent, H. D. Deng, D. H. Alsem, Y.-S. Yu, N. J. Salmon, D. A. Shapiro, P. R. Unwin and W. C. Chueh, *Nature*, 2021, 593, 67-73.
- 56. A. Sheelam and K. Ramanujam, *Electrochim. Acta*, 2016, **216**, 457-466.
- 57. T. Kitazawa, K. Yaji, K. Shimozawa, H. Kondo, T. Yamanaka, H. Yaguchi, Y. Ishida, K. Kuroda, A. Harasawa, T. Iwahashi, Y. Ouchi, F. Komori, S. Shin and K. Kanai, *Adv. Mater. Interfaces*, 2020, **7**, 2000524.
- M. R. Lichtenthaler, F. Stahl, D. Kratzert, L. Heidinger, E. Schleicher, J. Hamann, D. Himmel, S. Weber and I. Krossing, Nat. Commun., 2015, 6, 8288.
- 59. J. Qian, T.-T. Li, Y. Hu and S. Huang, *Chem. Commun.*, 2017, **53**, 13027-13030.
- M. Zhao, W. Yuan and C. M. Li, J. Mater. Chem. A, 2017, 5, 1201-1210.
- 61. L. Shahriary and A. A. Athawale, *J. Solid State Electrochem.*, 2015, **19**, 2255-2263.

- A. Badreldin, J. Abed, N. Hassan, A. El-Ghenymy, W. Suwaileh, Y. Wubulikasimu, Z. K. Ghouri, K. Youssef, D. Kumar, K. Elsaid, E. H. Sargent and A. Abdel-Wahab, Appl. Catal. B: Environ., 2023, 330, 122599.
- 63. M. F. Bekheet, M. R. Schwarz, S. Lauterbach, H.-J. Kleebe, P. Kroll, R. Riedel and A. Gurlo, *Angew. Chem. Int. Ed.*, 2013, **52**, 6531-6535.
- 64. D. B. Buchholz, Q. Ma, D. Alducin, A. Ponce, M. Jose-Yacaman, R. Khanal, J. E. Medvedeva and R. P. H. Chang, *Chem. Mater.*, 2014, **26**, 5401-5411.
- Z. Wan, Q. He, Y. Qu, J. Dong, E. Shoko, P. Yan, T. Taylor Isimjan and X. Yang, J. Electroanal. Chem., 2022, 904, 115928.
- Z. Zhu, X. Yang, J. Liu, M. Zhu and X. Xu, Carbon Energy, 2023, 5, e327.
- M. Zhao, H. Li, W. Yuan and C. M. Li, ACS Appl. Energy Mater., 2020, 3, 3966-3977.
- K. Kawashima, R. A. Márquez, Y. J. Son, C. Guo, R. R.
 Vaidyula, L. A. Smith, C. E. Chukwuneke and C. B. Mullins, ACS Catal., 2023, 13, 1893-1898.
- 69. G. Kresse and J. Hafner, *Phys. Rev. B*, 1993, **47**, 558-561.
- G. Kresse and J. Furthmüller, *Phys. Rev. B*, 1996, **54**, 11169-11186.
- 71. K. Lejaeghere, G. Bihlmayer, T. Björkman, P. Blaha, S. Blügel, V. Blum, D. Caliste, I. E. Castelli, S. J. Clark, A. Dal Corso, S. de Gironcoli, T. Deutsch, J. K. Dewhurst, I. Di Marco, C. Draxl, M. Dułak, O. Eriksson, J. A. Flores-Livas, K. F. Garrity, L. Genovese, P. Giannozzi, M. Giantomassi, S. Goedecker, X. Gonze, O. Grånäs, E. K. U. Gross, A. Gulans, F. Gygi, D. R. Hamann, P. J. Hasnip, N. A. W. Holzwarth, D. Iuşan, D. B. Jochym, F. Jollet, D. Jones, G. Kresse, K. Koepernik, E. Küçükbenli, Y. O. Kvashnin, I. L. M. Locht, S. Lubeck, M. Marsman, N. Marzari, U. Nitzsche, L. Nordström, T. Ozaki, L. Paulatto, C. J. Pickard, W. Poelmans, M. I. J. Probert, K. Refson, M. Richter, G.-M. Rignanese, S. Saha, M. Scheffler, M. Schlipf, K. Schwarz, S. Sharma, F. Tavazza, P. Thunström, A. Tkatchenko, M. Torrent, D. Vanderbilt, M. J. van Setten, V. Van Speybroeck, J. M. Wills, J. R. Yates, G.-X. Zhang and S. Cottenier, Science, 2016, 351, aad3000.
- 72. J. P. Perdew, K. Burke and M. Ernzerhof, *Phys. Rev. Lett.*, 1996, **77**, 3865-3868.
- 73. Y. Hinuma, G. Pizzi, Y. Kumagai, F. Oba and I. Tanaka, *Comput. Mater. Sci.*, 2017, **128**, 140-184.
- 74. A. Togo and I. Tanaka, *Journal*, 2018, DOI: 10.48550/arXiv.1808.01590, arXiv:1808.01590.
- V. Wang, N. Xu, J.-C. Liu, G. Tang and W.-T. Geng, Comput. Phys. Commun., 2021, 267, 108033.

All the original data related to the manuscript can be available upon request